Am J Physiol Heart Circ Physiol
281: H253–H265, 2001.

Patterns of wave break during ventricular fibrillation in isolated swine right ventricle

MOON-HYOUNG LEE,*[1] ZHILIN QU,*[2] GREGORY A. FISHBEIN,[1] SCOTT T. LAMP,[2] EUGENE H. CHANG,[1] TOSHIHIKO OHARA,[1] OLGA VOROSHILOVSKY,[1] JONG R. KIL,[2] ALI R. HAMZEI,[1] NINA C. WANG,[1] SHIEN-FONG LIN,[3] JAMES N. WEISS,[2] ALAN GARFINKEL,[2] HRAYR S. KARAGUEUZIAN,[1] AND PENG-SHENG CHEN[1]

[1]*Division of Cardiology, Department of Medicine, Cedars-Sinai Medical Center, and* [2]*Division of Cardiology, Departments of Medicine and Physiology and Physiological Science, University of California School of Medicine, Los Angeles, California 90048; and* [3]*Department of Physics and Astronomy, Vanderbilt University, Nashville, Tennessee 37235*

Received 16 March 2000; accepted in final form 22 February 2001

Lee, Moon-Hyoung, Zhilin Qu, Gregory A. Fishbein, Scott T. Lamp, Eugene H. Chang, Toshihiko Ohara, Olga Voroshilovsky, Jong R. Kil, Ali R. Hamzei, Nina C. Wang, Shien-Fong Lin, James N. Weiss, Alan Garfinkel, Hrayr S. Karagueuzian, and Peng-Sheng Chen. Patterns of wave break during ventricular fibrillation in isolated swine right ventricle. *Am J Physiol Heart Circ Physiol* 281: H253–H265, 2001.—Several different patterns of wave break have been described by mapping of the tissue surface during fibrillation. However, it is not clear whether these surface patterns are caused by multiple distinct mechanisms or by a single mechanism. To determine the mechanism by which wave breaks are generated during ventricular fibrillation, we conducted optical mapping studies and single cell transmembrane potential recording in six isolated swine right ventricles (RV). Among 763 episodes of wave break (0.75 times$\cdot s^{-1}\cdot cm^{-2}$), optical maps showed three patterns: 80% due to a wave front encountering the refractory wave back of another wave, 11.5% due to wave fronts passing perpendicular to each other, and 8.5% due to a new (target) wave arising just beyond the refractory tail of a previous wave. Computer simulations of scroll waves in three-dimensional tissue showed that these surface patterns could be attributed to two fundamental mechanisms: head-tail interactions and filament break. We conclude that during sustained ventricular fibrillation in swine RV, surface patterns of wave break are produced by two fundamental mechanisms: head-tail interaction between waves and filament break.

reentry; mapping; electrophysiology; action potentials; restitution

ON THE BASIS OF COMPUTER SIMULATIONS, Moe et al. (26) proposed the multiple wavelet hypothesis of fibrillation, in which they postulated that cardiac fibrillation is due to the presence of a number of independent wavelets. The wavelets appear to propagate randomly through the myocardium and are maintained by seemingly spontaneous wave splitting (wave break) that constantly regenerates new daughter wavelets. Subsequent experimental studies demonstrated the presence of multiple wavelets in both atrial (7, 12, 19) and ventricular fibrillation (VF) (16, 17, 21). From activation maps of the surface of the heart, two patterns of wave break have been characterized: wave break when two waves intersect, often perpendicularly (5, 21), and wave break when a wave front collides with the refractory tail of a preceding spontaneous (13) or paced (10, 27) activation. A weakness of electrode mapping studies is that the repolarization patterns of the wave fronts cannot be determined (5). The wave front-wave tail interaction can only be deduced based on the patterns of activation not by direct visualization. Most of the optical mapping studies of the wave break formation were based on the interactions between wave fronts induced by pacing (10, 27) and not on the study of spontaneous occurring wave fronts during Wiggers' stage II VF. Because of these limitations, it is unclear which of these mechanisms of wave break formation are most important and, indeed, whether they really are distinct mechanisms rather than manifestations on the surface of the heart of wave break occurring deeper in the tissue by a common mechanism. In the present study, we used high-density optical mapping techniques (23) and single cell transmembrane potential (TMP) recordings to study both the activation and repolarization patterns during VF in isolated swine right ventricles (RV) (17) and to quantify the frequency of different surface patterns of wave break. We then performed computer simulations of three-dimensional (3-D) tissue to determine whether or not the same surface patterns could be reproduced and to investigate the underlying mechanisms of wave break.

METHODS

Optical mapping of swine RV. The research protocol was approved by the institutional animal care and use committee and followed the guidelines of the American Heart Associa-

*M.-H. Lee and Z. Qu contributed equally to this study.

Address for reprint requests and other correspondence: P.-S. Chen, Rm. 5342, CSMC, 8700 Beverly Blvd., Los Angeles, CA 90048 (E-mail: chenp@cshs.org).

The costs of publication of this article were defrayed in part by the payment of page charges. The article must therefore be hereby marked "*advertisement*" in accordance with 18 U.S.C. Section 1734 solely to indicate this fact.

tion. Six farm pigs (25–32 kg) of either sex were used in the study. The details of this model have been reported elsewhere (17). Briefly, the RV was isolated, perfused with oxygenated Tyrode solution, and placed in a tissue bath with either the epicardium ($n = 3$) or endocardium ($n = 3$) facing up for optical mapping. The pseudoelectrocardiogram was monitored and recorded by a pair of widely spaced bipolar electrodes.

The optical mapping system used in the present study was similar to the one described previously (23) except that the stimulating light was delivered to the tissue with fiber-optic bundles (model A08550, Fostec; Auburn, NY) through an interference filter (500 ± 30 nm, Omega Optical; Brattleboro, VT) from a stabilized 250-W tungsten halogen lamp (model 66196, Oriel; Stratford, CT). The RV were stained for 20 min with 1–2 μM pyrimidine 4-(2-(6-(dibutylamino)-2-naphthalenyl) ethenyl)-1-(3-sulfopropyl) hydroxide (di-4-ANEPPS; Molecular Probes) added to the Tyrode solution. The induced fluorescence was collected through a 600-nm long-pass glass filter (R60, Nikon; Tokyo, Japan) and a 25-mm/f 0.85 video lens (Fujinon CF25L, Fuji Photo Optical; Omiya City, Japan) with a 12-bit digital charge-coupled device camera (CA-D1–0256T, Dalsa; Ontario, Canada) programmed to sample at 3.75-ms intervals. The camera acquired data from 96 × 96 sites simultaneously over a 35 × 35-mm^2 area, resulting in a spatial resolution of 0.36 × 0.36 mm^2/pixel. However, due to the need for temporal and spatial averaging to reduce noise (see below), the effective resolution was reduced. The face plate of the camera was cooled with an ethylene-glycol coolant from a refrigerated water bath to 15°C. The digital images were transferred to a personal computer with a frame grabber (IC-PCI-DIG16, Imaging Technology; Bedford, MA). During the experiment, the tissue was immobilized by pinning it to the base of the tissue chamber. Because the RV did not contract effectively during VF, we did not use electromechanical uncouplers in this study.

TMPs were recorded from a surface cell using standard techniques (17). The digitization rate was 5 kHz with 12 bits of accuracy.

All hearts developed VF during excision. VF continued in the excised RV (17). Continuous TMP recordings were made during VF for 30–60 s. The RV was then stained with di-4-ANEPPS, and the TMP recordings were repeated. The patterns of activation of VF were acquired by the charge-coupled device camera.

Signal processing. The optical signals were temporally filtered and spatially averaged to reduce noise. For temporal filtering, we applied a five-point time median filter to each pixel. We took the original first five data points (*frames 1*, *2*, *3*, *4*, and *5*), found the median value of those points, and used that as the new value for *point* (*frame*) *3*. We then took the next original five points (i.e., *frames 2*, *3*, *4*, *5*, and *6*), found the median value of those, and used that as the new value for *point 4*. We continued this exercise until the end of the data. We then took the tracing, inverted the data, and brought the baseline down to zero, which was defined by the average of the five lowest fluorescent values recorded by that pixel. Afterward, we range normalized each pixel. We found the five lowest and five highest points and took the average of those numbers. We then adjusted the fluorescent value of each pixel by the same amount so that the highest pixel value was 255 and the lowest was 0. For each pixel on the frame, we then averaged the fluorescent values of the pixel and its eight surrounding pixels. We used this average as the new value for the pixel. After those averaging procedures were completed, we repeated the procedure for a second time. At that time, we rezeroed the signal by bringing the baseline down to zero, defined by the average of the five lowest points of each pixel. We then range normalized the signals again. The maximal signal amplitude was coded white, representing a fully depolarized state. The minimum signal amplitude was coded black, representing a fully repolarized state. Each pixel was then assigned a shade of gray between white and black.

For the computer-assisted automatic detection of wave break, we defined the occurrence of wave break in a propagating wavelet as the point where the activation wave front and the repolarization wave back joined together. The computer first found every adjacent pair of pixels in the frame that crossed the average value of the data. If the intensity of the data on which the line coincides is increasing, that edge is identified as the wave front and colored red. Otherwise, if it is decreasing, the edge is identified as the wave back and colored blue (25). The point where the red line meets the blue line is the wave break. Each of these wave breaks was further analyzed by visual inspection of consecutive frames. We included in analyses the wave breaks occurring in large and coherent wave fronts. Excluded from analyses were the wave fronts that changed from blue to red and vice versa from frame to frame or the appearance of red and blue dots in close vicinity, forming a mosaic pattern. We also excluded wave breaks if there was no continuous propagation of the red line or continued repolarization of the blue line around the wave break site over at least two consecutive frames. Because of these selection criteria, the absolute number of wave breaks reported in this paper might have underestimated the real quantity of wave breaks in VF. However, the wave breaks analyzed are likely to be true wave breaks.

We also generated color isochronal maps based on the location of wave fronts at each frame. First, a start frame and an end frame are selected by the user. For example, we chose *frames 241–259*. Second, the amount of frames to be skipped to get a new color is selected by the user. For example, we chose three. Third, the program generates on the screen isochronal lines according to the user's chosen criteria. In this case, the program identified the location of the activation wave fronts in *frames 241*, *242*, and *243* and labeled those isochronal lines red. The areas between the red lines were filled with red color. The program then switched to orange to draw isochronal lines for *frames 244*, *245*, *246*, and so on. At this point, the areas between the red lines were red, the areas between the orange lines were orange, and so on. The areas between two colors were left blank. Therefore, there were gaps of colors on the map. The program then filled in the gaps between adjacent colors with one color halfway across and the other color the rest of the way across.

The single cell TMP recorded by glass microelectrode was analyzed to determine the diastolic interval [DI; the time between 90% of repolarization of the preceding action potential (AP) to the upstroke of the current AP] and the AP duration (APD) from upstroke to 90% repolarization (APD_{90}). Details of the algorithm have been published elsewhere (17). The DI and APD measured by glass microelectrode may not be the same as those measured by optical mapping techniques. Each pixel of the optical map represents fluorescent changes of hundreds of cells. Because these cells may not activate and repolarize in phase, the DI is often nonexistent on optical signals.

The APD restitution curve was created by plotting APD_{90} against the preceding DI. The restitution curve was generated by an exponential fit using ORIGIN 5.0 (Microcal Software; Northampton, MA). ORIGIN was also used for statistical analyses. Results are expressed as means ± SD. A P value of <0.05 was considered significant.

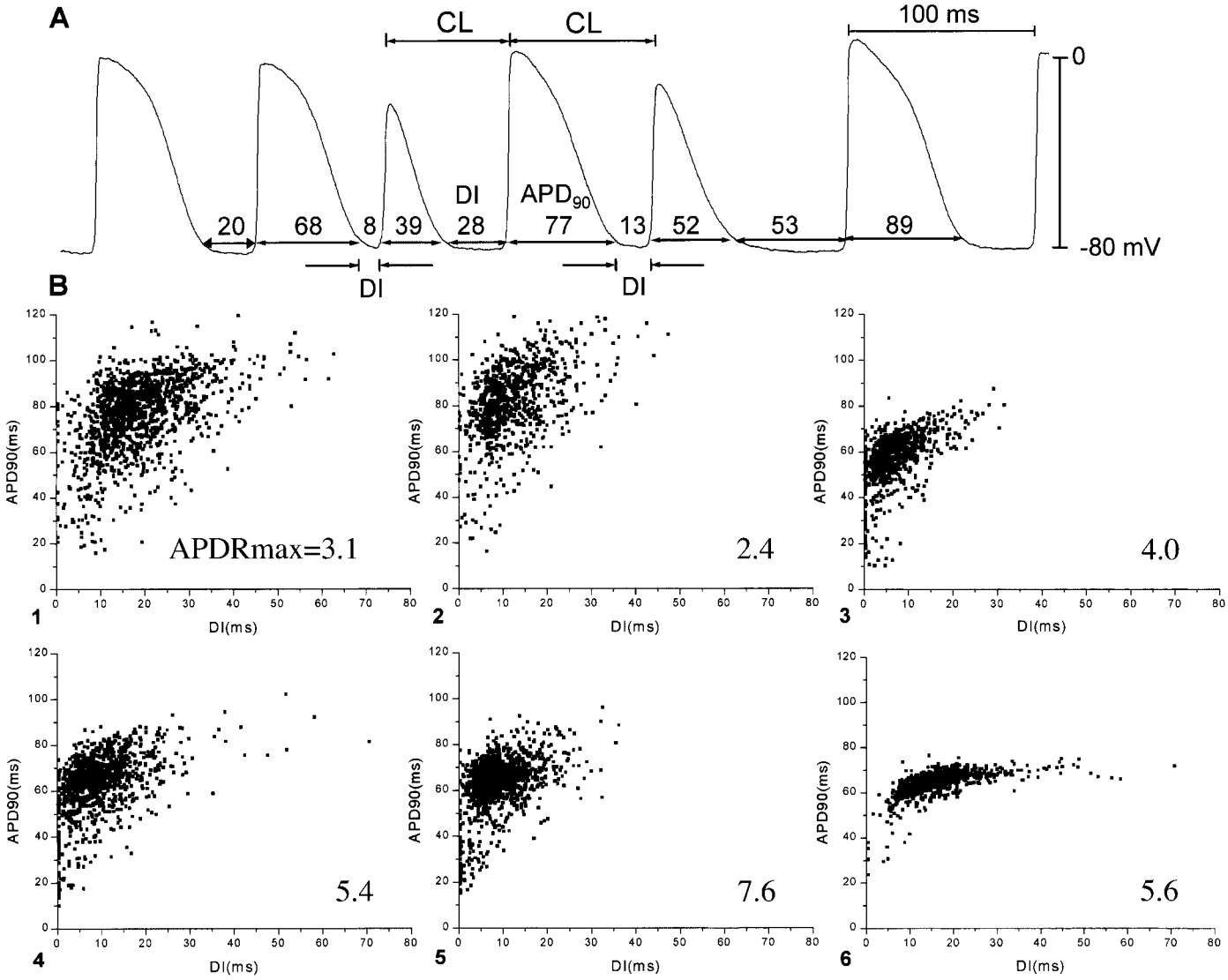

Fig. 1. Action potentials (AP) recorded during ventricular fibrillation (VF) and AP duration (APD) restitution curves during VF in 6 isolated swine right ventricles (RV). *A*: typical transmembrane potential (TMP) recording showing that APD is positively related to the preceding diastolic interval (DI). *B*: APD restitution characteristics in all 6 tissues (*1–6*). The maximum slope of the APD restitution curve ($APDR_{max}$) is identified in each of the 6 tissues. CL, cycle length; APD_{90}, APD from upstroke to 90% repolarization.

Computer simulation. The partial differential equation for cardiac conduction is as follows (11)

$$\partial_t V = -I_{ion}/C_m + \nabla \times \tilde{\mathbf{D}} \nabla V \quad (1)$$

where V is the TMP, C_m the membrane capacitance, and t is time. I_{ion} is the total ionic current density of the membrane. The diffusion tensor $(\tilde{\mathbf{D}}) = \tilde{\boldsymbol{\sigma}}/S_v C_m$, where $\tilde{\boldsymbol{\sigma}}$ is the conductivity tensor and S_v is the surface-to-volume ratio of the cell. We used no flux boundary condition (11): $\hat{\mathbf{n}} \times \tilde{\mathbf{D}} \nabla V = 0$, where $\hat{\mathbf{n}}$ is the unit vector normal to the boundary. We assumed the fibers were parallel and uniform in the x-y plane but rotated along the z-direction. Therefore, $\tilde{\mathbf{D}}$ had the following matrix structure (11)

$$\tilde{\mathbf{D}} = \begin{pmatrix} \mathbf{D}_{xx} & \mathbf{D}_{xy} & 0 \\ \mathbf{D}_{yx} & \mathbf{D}_{yy} & 0 \\ 0 & 0 & \mathbf{D}_{zz} \end{pmatrix} \quad (2)$$

where

$$\begin{aligned} \mathbf{D}_{xx} &= D_{\parallel} \cos^2 \theta(z) + D_{\perp} \sin^2 \theta(z) \\ \mathbf{D}_{yy} &= D_{\parallel} \sin^2 \theta(z) + D_{\perp} \cos^2 \theta(z) \\ \mathbf{D}_{xy} &= \mathbf{D}_{yx} = (\mathbf{D}_{\parallel} - D_{\perp}) \cos \theta(z) \sin \theta(z) \\ \mathbf{D}_{zz} &= D_{\perp} \end{aligned} \quad (3)$$

$D_{\parallel}$ is the diffusion constant along the fiber direction, and $D_{\perp}$ is the transverse diffusion constant. We used $D_{\parallel} = 0.001$ cm^2/ms and $D_{\perp} = 0.0002$ cm^2/ms. $\theta(z)$ is the angle between the fiber and the x-axis. We used a uniform fiber rotation angle, $\theta(z) = \alpha z$, where α is a constant. I_{ion} in *Eq. 1* was taken from the phase 1 Luo-Rudy (LR1) AP model (24). We varied some parameters to change the APD and APD restitution. The parameters were selected so that APD restitution was steep enough to cause spontaneous wave break in the simulated 3-D tissue when the thickness exceeded 0.4 cm. We

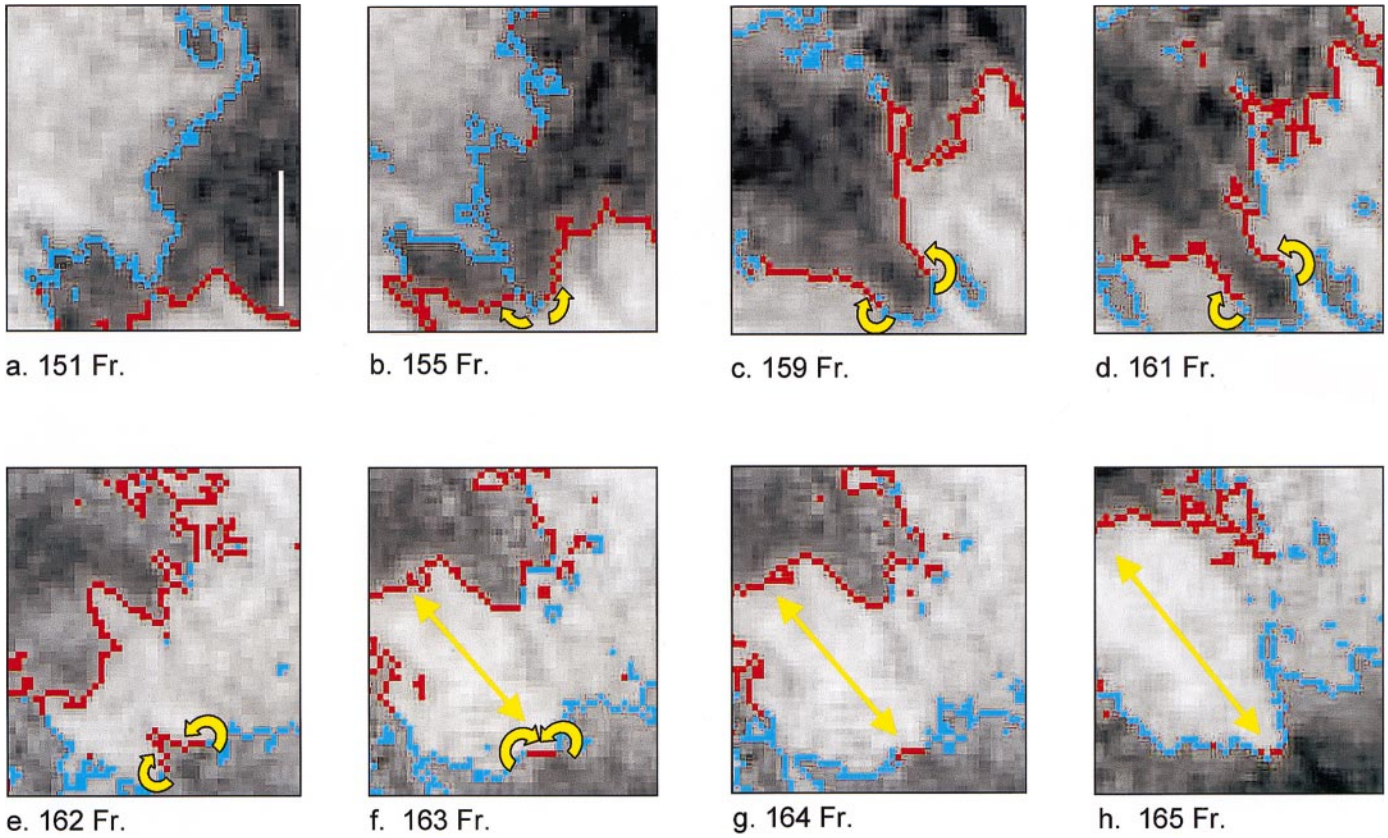

Fig. 2. The wave break and initiation of reentry by a wave front encountering the trailing edge of refractoriness from a neighboring wave. *Frames a–h* show sequential wave maps recorded by the optical mapping system during VF. The red line denotes the wave front, and the blue line denotes the wave tail. Curved yellow arrows indicate the direction of the reentrant wave fronts. The double-headed yellow arrow shows two waves traveling in opposite directions. The white vertical bar in *frame a* = 1 cm.

used $\bar{G}_{Na}$ = 16 mS/cm^2, $\bar{G}_K$ = 0.0423 mS/cm^2, and $\bar{G}_{Si}$ = 0.047 mS/cm^2, where $\bar{G}$ is maximum value of the channel conductance. We also sped up the Ca^{2+} kinetics, i.e., $\tau_d \rightarrow 0.5\tau_d$ and $\tau_f \rightarrow 0.5\tau_f$. τ_d and τ_f are the time constants for the recovery of activation and inactivation, respectively, of the L-type calcium channel.

We used our advanced numerical method (28) to integrate *Eq. 1* with time steps varying from 0.02 to 0.2 ms. The space step was 0.015 cm. The tissue size was 4.8 × 4.8 × 0.9 cm^3. (In comparison, the swine RV has a thickness of ~5–7 mm.) The total fiber rotation angle was θ = 120°, i.e., α = 13.3°/mm. The simulation was started with a single intact scroll wave. Simulations were carried out in the San Diego Supercomputer Center.

RESULTS

APD restitution during VF. To determine the APD restitution curve, DI and APD_{90} were calculated from conventional single cell TMP during VF. The average cycle length during VF was 79 ± 17 ms, and the average DI was 12 ± 8 ms. Figure 1*A* shows typical TMPs recorded during VF. The APD restitution curve was created by plotting APD_{90} against the preceding DI (Fig. 1*B*). The maximum slope of the APD restitution curves ranged from 2.4 to 7.6.

Surface patterns of wave break during VF. During sustained VF, multiple wavelets coexisted. A total of 763 episodes of wave break were observed in 83 s of VF. Thus new wave break occurred 0.75 times·s^{-1}·cm^{-2}. In 612 episodes (80%), wave break was caused by a wave front encountering the trailing edge of refractoriness from a previous activation or neighboring wave. Figure 2 shows an example. *Frame a* shows a convex wave front at the bottom of the mapped tissue moving upward. The central portion of the convex wave front encounters residual refractoriness left over by a previous activation (shown by the blue line). Unable to propagate into the refractory region, the new wave front breaks in its central portion, splitting into two daughter wavelets (*frame b*). The two daughter wavelets turn on themselves, forming a figure-8 (yellow arrows in *frames b–f*) around the site of the initial wave break. The two wavelets then collide and fuse, forming a central common pathway, which then propagates in both directions (double-headed yellow arrows, *frames f–h*). Reentry continues after *frame h* to complete two cycles of the figure-8 pattern. Note that in *frame f* there is a mosaic pattern in the right upper quadrant. The junctions of the red and blue dots in that region were not included for wave break analyses.

Figure 3*C* shows an isochronal map of the figure-8 reentrant loop shown in Fig. 2. The color isochrones indicate the locations of the activation wave fronts at

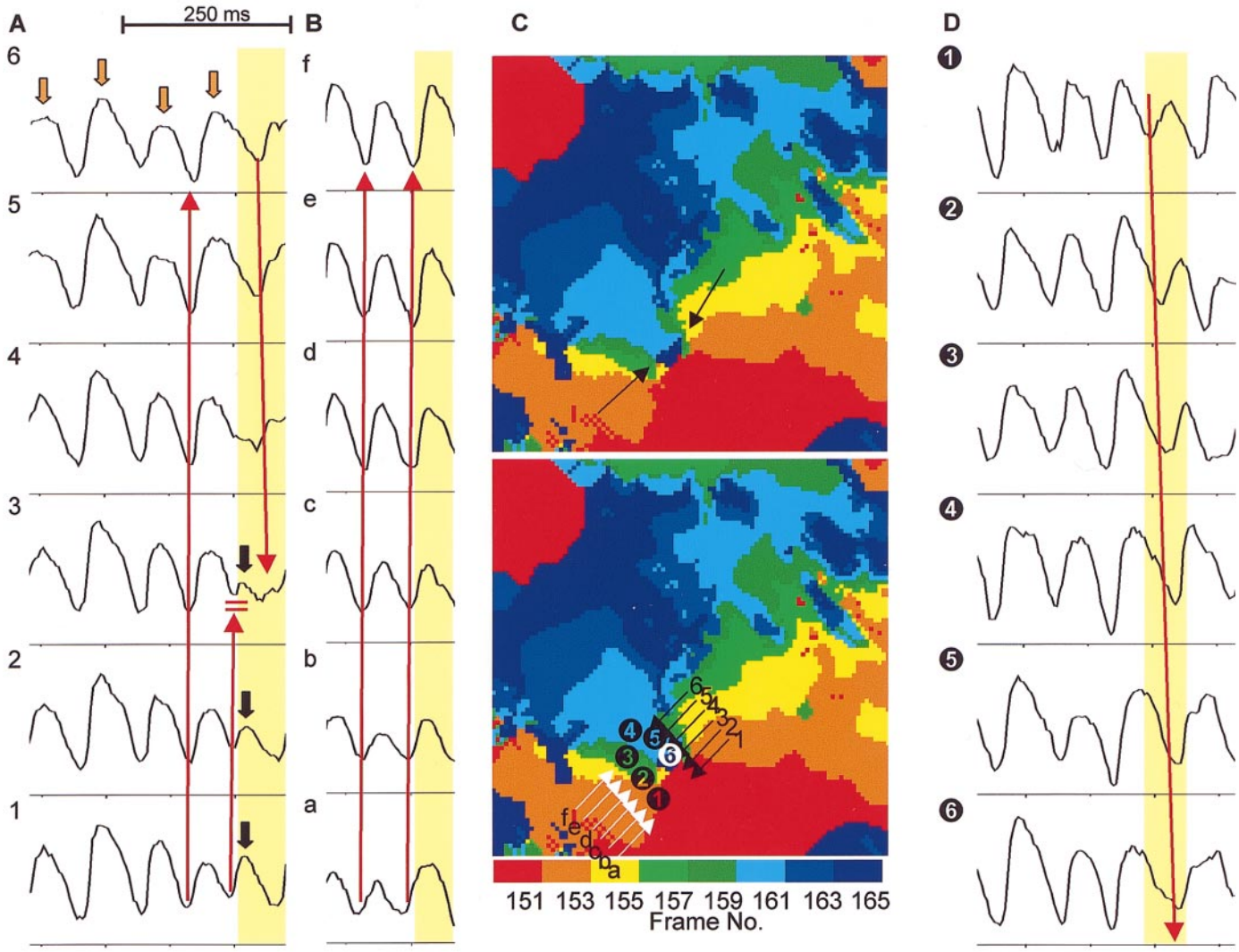

Fig. 3. Isochronal map (*C*) and optical potentials (*A*, *B*, and *D*) of wave break. This is the same episode as that shown in Fig. 2. *C*, *top*: an isochronal map with arrows pointing to the two wave break sites. *C*, *bottom*: the same isochronal map with numbers and letters corresponding to the recordings shown in *A*, *B*, and *D*. The yellow segments in *A*, *B*, and *D* indicate the time window during which the activations in *frames a–h* of Fig. 2 were registered.

the frame number shown on the color bar. There are eight colors, representing activation of 15 frames (56.25 ms) of data. Therefore, each color represents 7 ms of activation. This isochronal map does not contain the first reentrant activation at *pixels 1* and *2* shown in Fig. 3*A*. Optical signals in Fig. 3 from selected sites (black and white thin arrows in *C*) are plotted in *A* and *B*, respectively. In Fig. 3*A*, optical signals in *site 6* (downward orange arrows) as well as in other sites show large APD oscillations preceding wave break. The patterns of wave fronts associated with APD oscillations were similar to each other. The first long red arrow indicates the smooth uninterrupted propagation of the wave front immediately before wave break. The short upward red arrow shows the wave break, which was associated with a progressive shortening of DI and APD and cessation of propagation in the central portion of the wave front (black thick arrows), leading to block (double horizontal red line segments). After wave break occurred, the wave traveled in the opposite direction (long downward red arrow). Figure 3*B* shows that the peripheral portion of the wave front kept propagating forward without a significant shortening of either DI or APD. Figure 3*D* shows optical signals from six different sites (numbers in circles) from one reentrant wave front (long red arrow) as indicated in *C* (*bottom*).

Perpendicular wave front intersection. In 86 episodes (11%), wave break was created by a wave front crossing roughly perpendicularly to the tail of another wave front, similar to that reported previously in the canine RV in vivo (21). Figure 4 shows an example. *Frames a–c* show the first wave front propagating from the lower right to the upper left corner. A second wave front arising at the bottom left of the mapped region (*frame a*) spread upward and to the right (*frames b* and

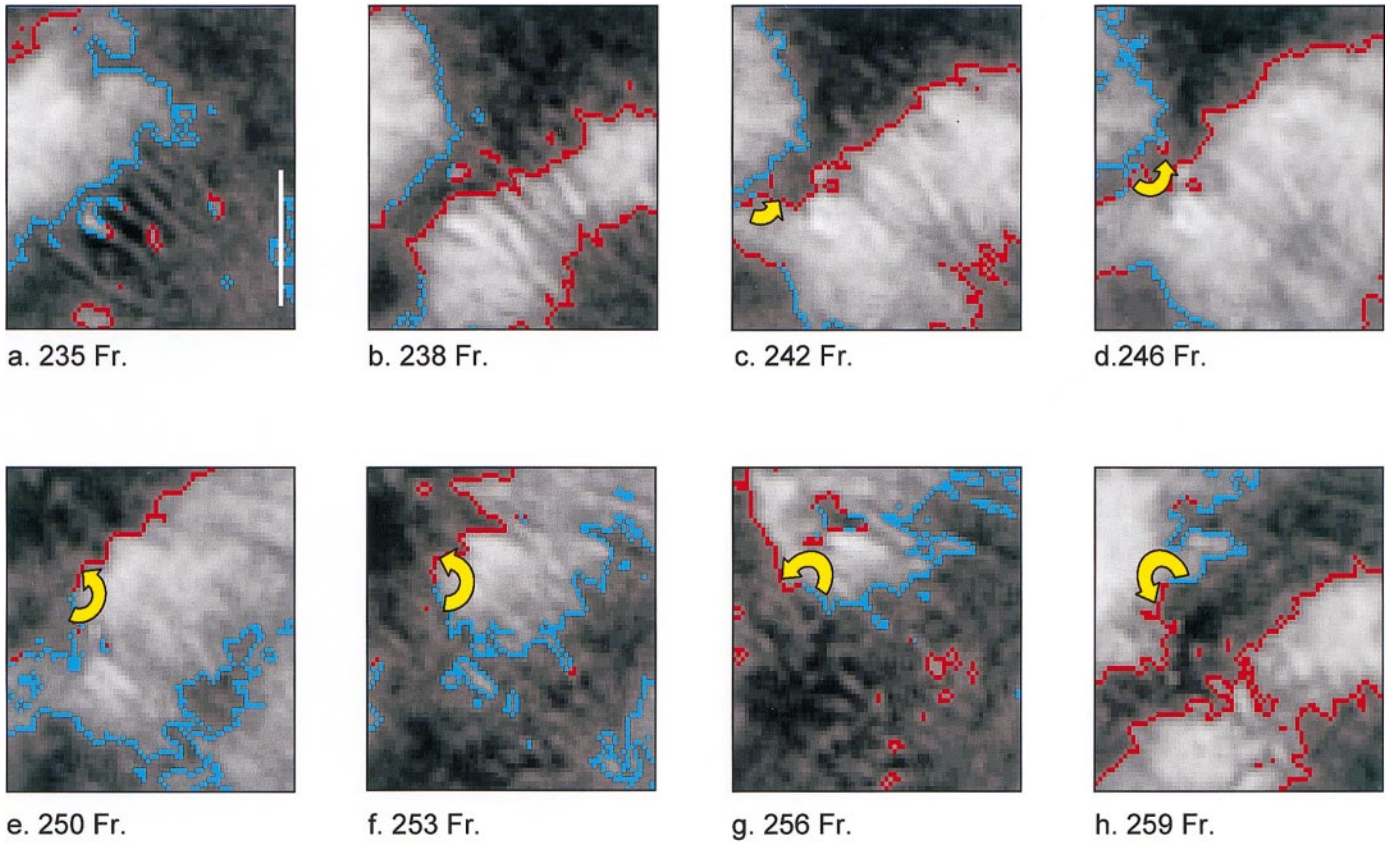

Fig. 4. The wave break and initiation of reentry by perpendicular interaction of two wave fronts. *Frames a–h* show sequential dynamic wave maps of activation and repolarization. The red line represents the wave front, and the blue line shows the refractory wave tail. Curved yellow arrows indicate the direction of wave front propagation.

c). As this wave front propagated, its perpendicular intersection with the residual refractoriness left over by the first wave front created wave breaks (*frames c* and *d*) and a counterclockwise reentrant wave front in the upper left quadrant of the mapped tissue (*frames d–h*).

Figure 5 shows the optical signals (*A* and *C*) and an isochronal map of reentry (*B*) for the episode shown in Fig. 4. The color isochrones indicate the locations of the activation wave fronts at the frame number shown on the color bar. There are seven colors, representing activation of 19 frames (71.25 ms) of data. Therefore, each color represents 10.2 ms of activation. Figure 5*A* shows optical signals from selected sites (black arrows) shown in *B* (*bottom*). The interaction was associated with progressively smaller potentials (black arrows in *A*), followed by cessation of propagation and wave break (double horizontal red line segments). Potentials just after wave break show that the direction of propagation (the long downward red arrow) is opposite to that before wave break. Figure 5*C* shows reentrant optical signals from six different sites as indicated in *B*.

Spontaneous focal wave fronts arising after the wave back of a previous wave. In 65 episodes (8.5%), we observed the generation of new wave breaks without apparent wave-wave interactions. Figure 6 shows a typical example in which a wave propagated from right to left (black arrows in *frames a–c*). At its wave back, a new target wave suddenly appeared on the right side (yellow arrows in *frames b–h*). It propagated into nonrefractory tissue to the right but was blocked as it propagated along the direction of the previous wave back. Two new wave breaks were created (white arrows in *frames i–l*). Figure 6*B* shows the optical signals recorded from six adjacent sites crossing the blue line (*A*, *frame a*). The cells at *sites 1–3* were in late phase 2 to early phase 3 repolarization. In contrast, the cells at *sites 4–6* were fully recovered. This is where the new activation arose to propagate rightward.

TMPs near the site of wave break. TMP recordings registered by glass microelectrodes were compared with the patterns of activation registered by the optical mapping system. Outside of the region of wave break (>2 mm away), AP amplitude, APD, the maximum change in voltage over time (dV/dt_{max}), and DI averaged 54 ± 16 mV, 62 ± 16 ms, 33 ± 19 V/s, and 11 ± 8 ms, respectively. In five episodes, wave break occurred within 2 mm of the microelectrode recording site, and TMPs showed significant ($P < 0.001$ for all comparisons) reductions in AP amplitude (31 ± 15 mV), duration (36 ± 13 ms), dV/dt_{max} (11 ± 7 V/s), and DI (5 ± 4 ms). Figure 7 shows the single cell TMP (*left*) and the fluorescent changes (*right*) at the site of wave breaks. A good correlation between wave break sites and diminished AP (27) supports the validity of our automated analysis for detecting wave fronts, wave backs, and wave break locations (2).

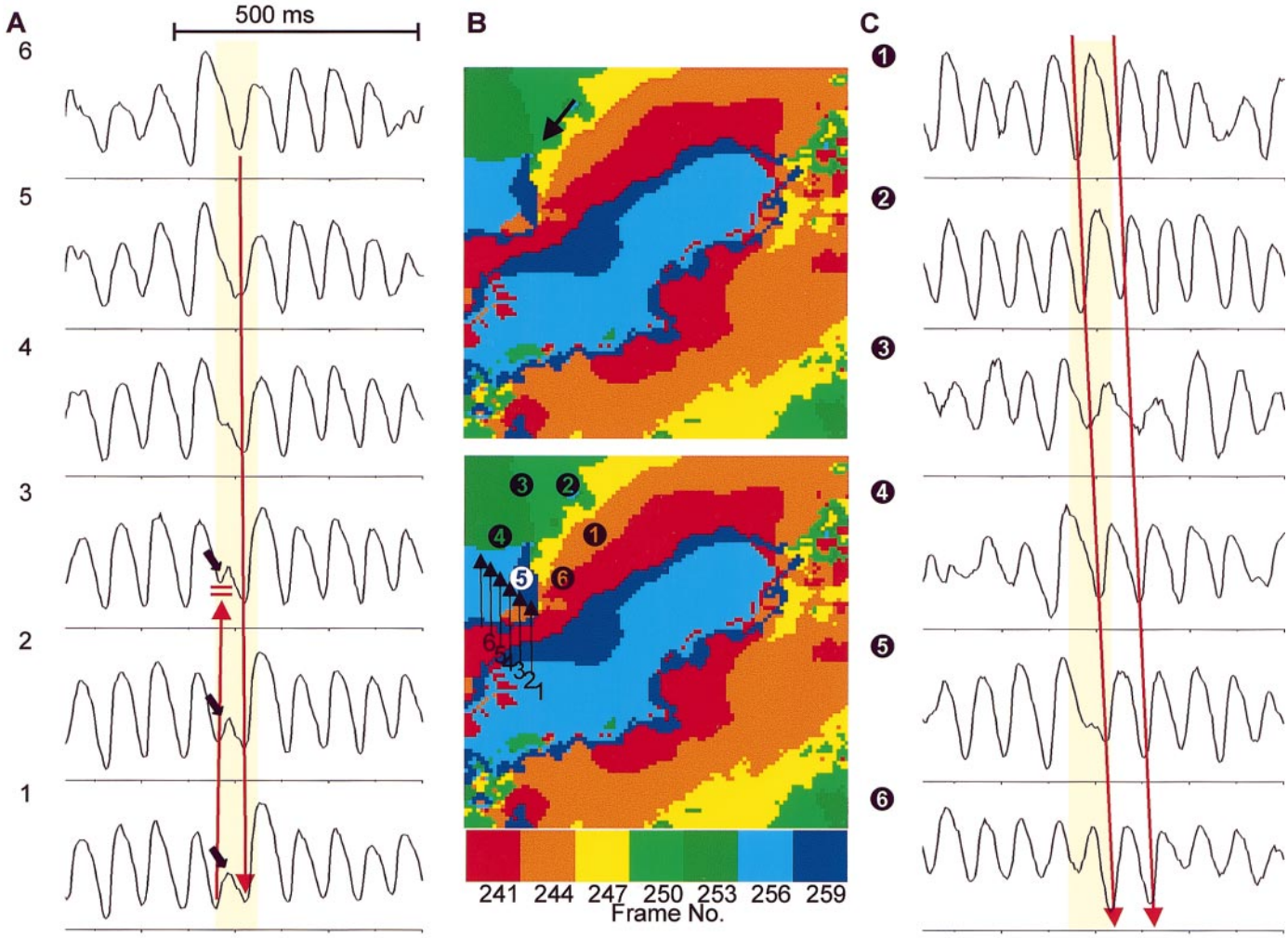

Fig. 5. Isochronal map (*B*) and optical signals (*A* and *C*) of wave break associated with the perpendicular interaction of two waves. This is the same episode as that shown in Fig. 4. The arrow in *B*, *top*, shows the site of wave break. *B*, *bottom*, shows the same isochronal map as *B*, *top*, with numbers and letters corresponding to the recordings shown in *A* and *C*. The yellow segments in *A* and *C* indicate the time window during which the activations in *frames a–h* of Fig. 4 were registered.

Computer simulations in 3-D cardiac tissue. To investigate the mechanisms responsible for the surface patterns of wave break observed experimentally, we performed computer simulations of fibrillation in 3-D tissue using the LR1 ventricular AP model. With steep APD restitution incorporated into the LR1 model, a scroll wave initiated in simulated tissue broke up to form multiple wavelets similar to fibrillation. Figures 8–10 illustrate that all three of the surface patterns of wave break observed experimentally were also observed on the surface of the simulated 3-D tissue. The first pattern, that of a wave front running into the trailing edge of refractoriness of a prior wave, is shown in Fig. 8. The second pattern, involving collision of perpendicular wave fronts (21), was also confirmed to be due to collision of a new wave front with a region of refractoriness left over from the first wave front (Fig. 9). Finally, the third pattern, the emergence of a focal-appearing wave front in the trail of a previous wave, was due to development of severe twist in the scroll filament, which broke off intramurally to form a scroll ring (Fig. 10). The initial target wave pattern was produced when the arm of the scroll wave arrived at the upper surface. Subsequently, the filament of the scroll ring drifted upward and intersected the surface, where it broke to create two new wave fronts.

The computer model does not contain papillary muscle or other endocardial structural inhomogeneities. The only inhomogeneity was the myocardial fiber orientation. Because the wave break occurs everywhere in the mapped region, it is not a phenomenon specific to the papillary muscle (18) or other endocardial structural inhomogeneities.

DISCUSSION

The main new finding in this study is that different surface patterns of wave break during fibrillation are all consistent with two fundamental mechanisms of

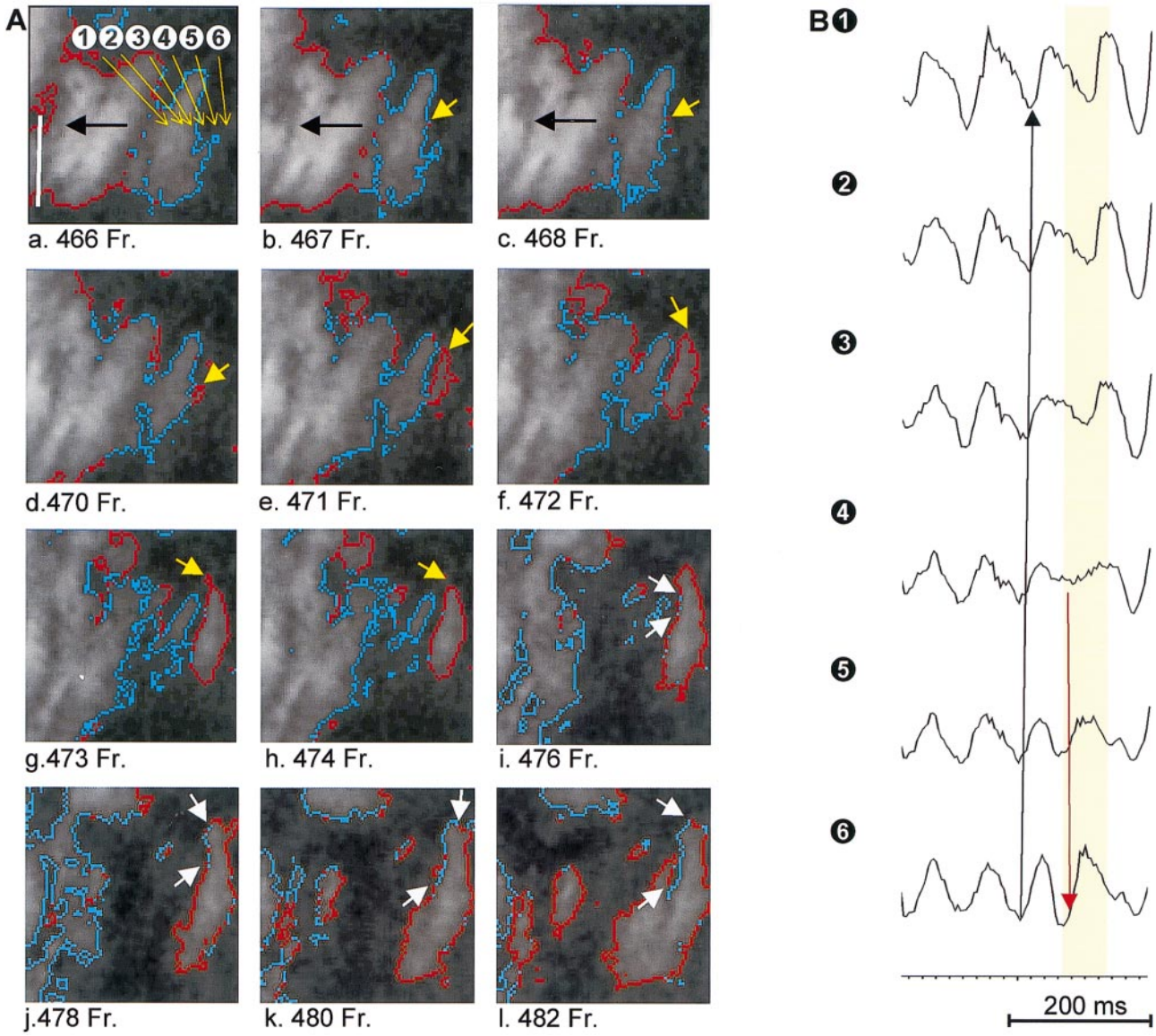

Fig. 6. Wave break occurring without wave-wave interaction. *A*: a wave propagating from right to left (black arrows). From the end of a previous wave back, a wavelet emerged and propagated in the opposite direction (yellow arrows) with new wave breaks (white arrows). *B*: optical signals. The numbers correspond to the locations shown in *A* (*frame a*). The yellow segment in *B* indicates the time window during which the activations in *frames a–l* in *A* were registered.

wave break, namely head-tail interactions when a wave front encounters residual refractoriness from a previous wave and filament break. The relation between local residual refractoriness and the formation of wave break is consistent with that proposed by Krinsky (20). The filament break, as first reported by Fenton and Karma (11), can also contribute to the generation of wave breaks. We arrived at this conclusion because, using a detailed AP model in simulated 3-D tissue, we could reproduce all of the surface patterns of wave break observed experimentally by these two mechanisms. The mechanism of wave break could be unequivocally identified in the simulation because events below the tissue surface, as well as the movement of the scroll filaments, could be directly monitored. Because the simulated 3-D tissue was completely homogeneous and isotropic, these data also suggest that fixed tissue anatomic and electrophysiological heterogeneities are not necessary to account for the observed patterns of wave break during fibrillation.

Spontaneous wave breaks and the perpetuation of VF. According to the multiple wavelet hypothesis (26), constant formation of new wavelets occurs through the process of wave splitting (wave break), in which a wave splits into new (daughter) wavelets. The process of wave break depends on the presence of electrophysiological heterogeneity, where regions of refractoriness, arising either dynamically from cardiac restitution properties or anatomically from obstacles or regional electrophysiological differences, cause localized propa-

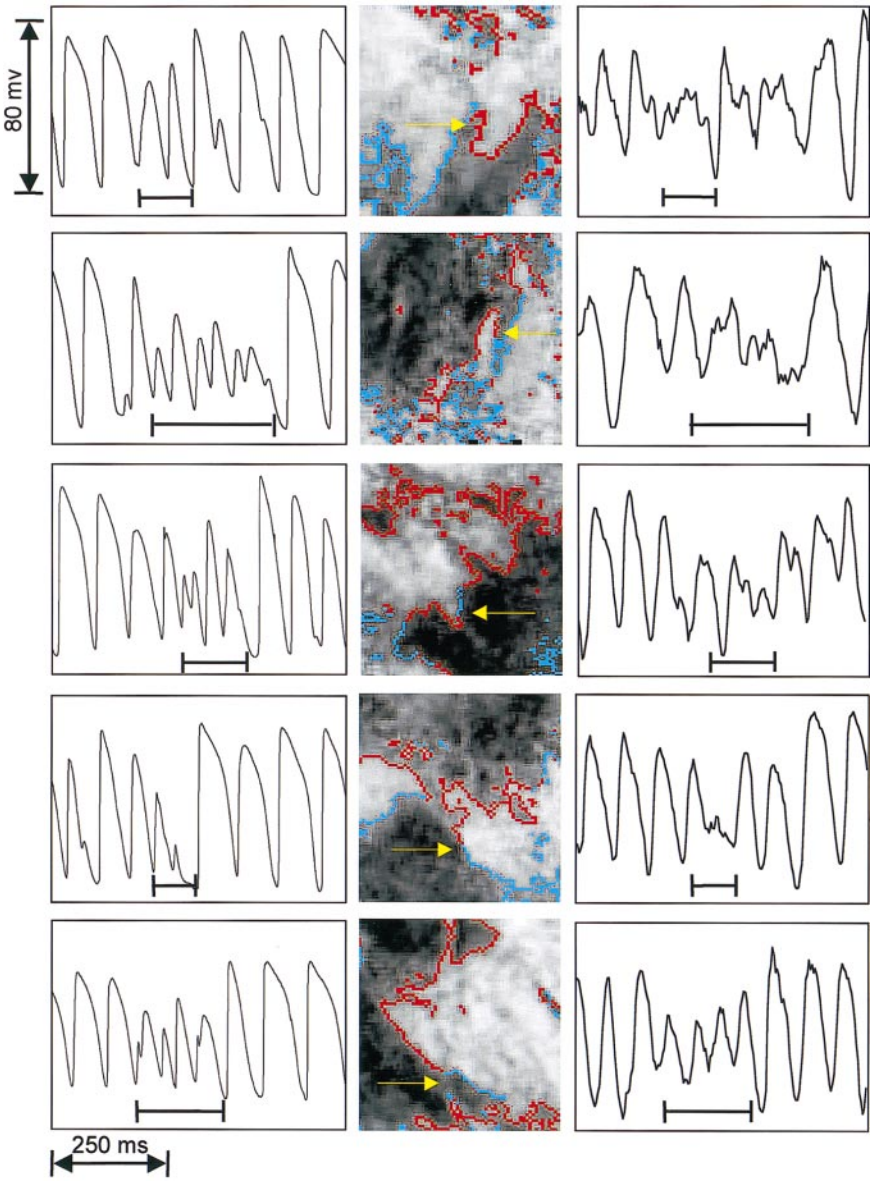

Fig. 7. Five examples of single cell TMP (*left*) and simultaneously registered fluorescent signals (*right*) at or near the wave break (*middle*). Each of the five rows represents one episode. The horizontal black bar indicates the times when wave break and reentrant wave fronts were recorded by the optical mapping system. The yellow arrows point to the site where TMP and fluorescent signals were recorded in each episode.

gation failure. Because the remaining portion of the wave fronts continues to propagate, it may result in a complete reentrant excitation (a spiral wave) (6, 9, 33). Therefore, the wave break provides new opportunities for reentry, perpetuating fibrillation. However, because of the complicated patterns of activation, not all wave breaks lead to the formation of complete reentry, no spiral wave or reentry is generated, and no phase singularity is detected. Therefore, the number of wave breaks determined in this study may not be equal to the number of phase singularities determined by other investigators (13).

Recently, optical mapping techniques (30) have allowed direct measurement of repolarization as well as activation during cardiac arrhythmias in animal models (8). Gray et al. (13) showed an example in which a wave front encountered refractory tissue, causing wave break. In the present study, we extended Gray et al.'s (13) observations by systematically analyzing the patterns of all wave breaks during sustained VF in perfused swine RV. We found that the mechanism described by Gray et al. (13) was the most common (80%), but, in addition, we observed two other surface patterns that occurred less frequently. In one pattern, the intersection of two perpendicular wave fronts produced wave break, as has been described previously by our group using multielectrode mapping (21). We hypothesized that the wave break occurs due to interaction of the second perpendicular wave front with the wave back of the first wave. The present study confirms that hypothesis. In another pattern, a focal target wave front appears in the wake of the passing wave, which develops wave break along the receding wave back of the previous wave as it expands. In the simulation, this pattern was observed when a twist developed in the filament of a scroll wave. The severe twist caused a section of the filament to bud off and form a separate scroll ring (circular filament), as shown in Fig. 10,

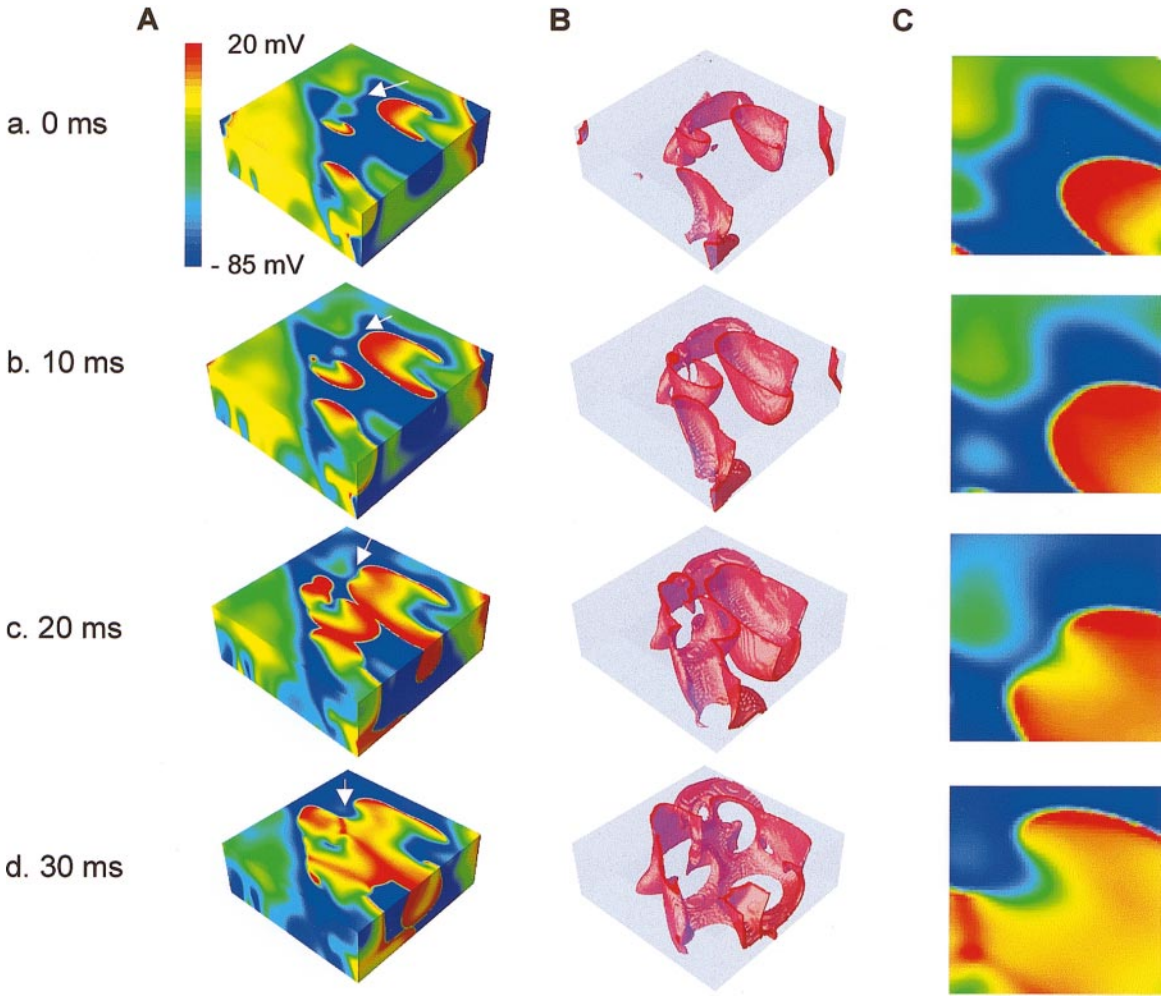

Fig. 8. Three-dimension simulation of wave break by a wave front running into the trailing edge of refractoriness. *A*: surface activation patterns (red = wave front, green = wave back) at the times indicated. The white arrows indicate the region where this mechanism of wave break occurs. *B*: corresponding scroll wave fronts in the tissue (red = rising membrane voltage). *C*: blowup of the region of wave break on the upper surface (near the white arrows in *A*). Residual refractoriness (green) was left over by a previous wave front, and when the next wave (red) encountered this refractory region, wave break occurred, generating two new scroll waves (compare with the experimental wave break in Fig. 2).

which subsequently migrated to the surface. Initially, the arm of the scroll emerged, producing the target wave. Subsequently, when the filament arrived at the surface, two new wave breaks appeared in the target wave. The formation of the new wave breaks was facilitated by preexisting refractoriness due to incomplete recovery of the previous wave front. In other simulations, we also observed that the twist in the original filament sometimes arrived at the surface and broke before a scroll ring had time to form, producing the same pattern observed experimentally.

Recovery of excitability and the formation of wave break. Given that these were normal hearts, the spatial heterogeneity in refractoriness was unlikely to be due to fixed anatomic or electrophysiological heterogeneity. Rather, it is more likely that the heterogeneity arose from dynamic processes, i.e., APD and conduction velocity restitution (4). Consistent with this idea, the slope of the APD restitution curve during VF was found to be steep (Fig. 1). Although there is a lot of scatter in the data points on the APD restitution curve, the best fit of an exponential curve to the data in Fig. 1, taking into consideration that APD restitution is not single valued during VF, gave a slope with a maximum value >1. A maximum slope of >1 is an important criteria for wave front instability during cardiac arrhythmias (31). A steep restitution curve contributes to the development of large changes of APD with small changes in DI (14, 15). When APD is shortened and small, the safety factor of propagation diminishes, resulting in wave break. Compatible with this hypothesis, extremely short DIs and APDs (black arrows in Fig. 3*A*) were noted before the occurrence of wave break in both the experiment and the simulation. If we deliberately made the slope of APD restitution more shallow by adjusting model parameters, spiral wave breakup and fibrillation could have been prevented (29).

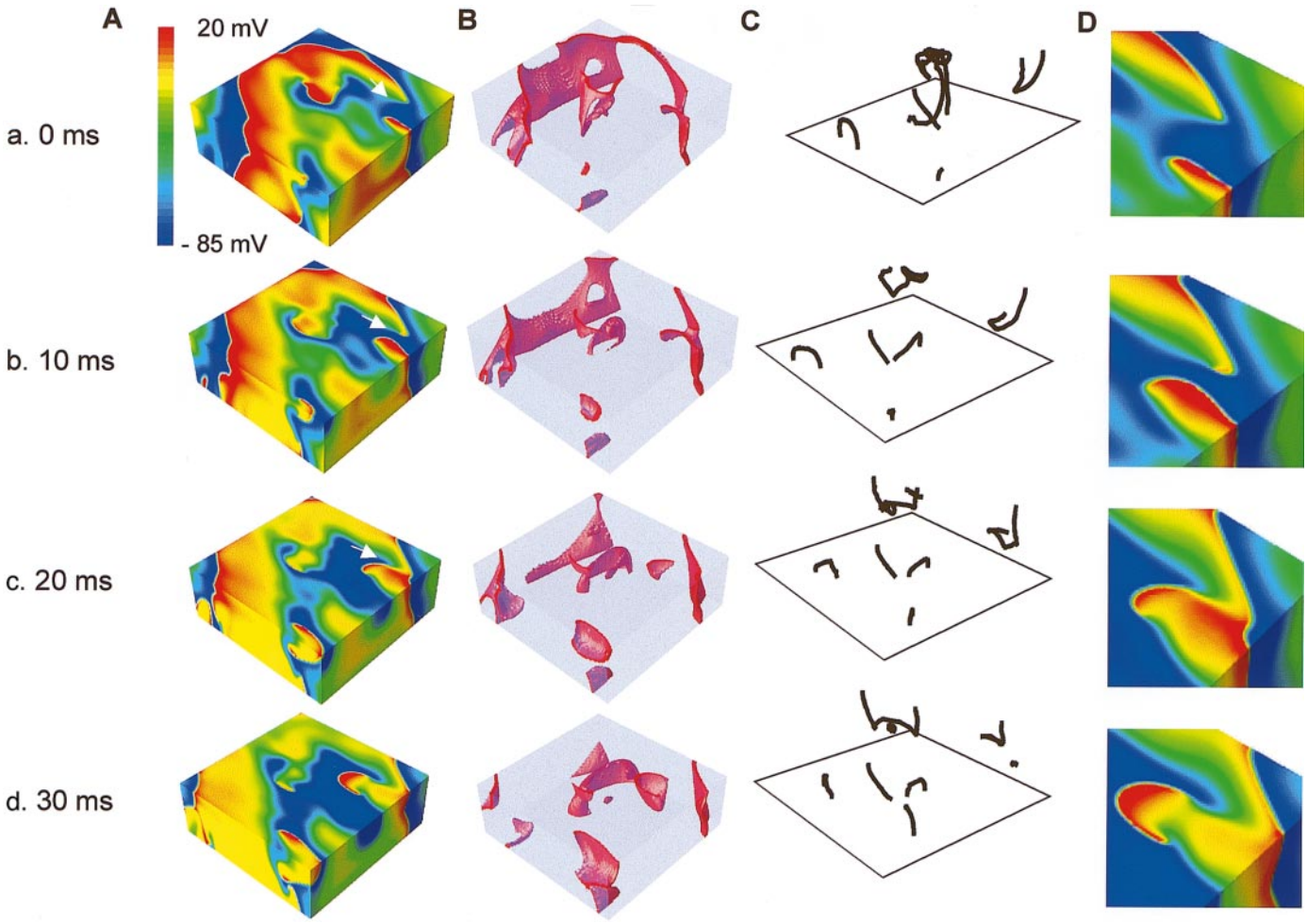

Fig. 9. Three-dimensional simulation of wave break by perpendicular intersection. The surface activation patterns (*A*), the scroll wave fronts in the tissue (*B*) and the filament (*C*), and a blowup of the region of wave break (*D*) (near the white arrows in *A*) are shown. A wave front propagated upward to the right, leaving an area of residual refractoriness at its wave back. A different wave front propagated upwards from the left, perpendicular to the first wave front. It encountered residual refractoriness, causing wave break and a new scroll filament to form (compare with the experimental wave break in Fig. 4).

Limitations of the study. Optical mapping is limited to the tissue surface, whereas wave break and reentry occurred in a 3-D structure. Therefore, we depended on simulations in 3-D tissue to infer what was happening beneath the surface in the RV preparations so that we could interpret the surface patterns of wave break. Thus we cannot exclude the possibility that other mechanisms of wave break may also be at work. This is particularly true for the filament break hypothesis because we were not able to map the filaments under the surface. An alternative hypothesis to explain the patterns seen in Fig. 6 is reflected reentry (1), which occurs when recovered tissues and the recovering or depolarized tissues are adjacent to each other. The differences of membrane potential results in excitation of the recovered tissue. Mapping study would show that a wave front (red) develops from the edge of repolarizing tissue (blue), as shown in Fig. 6. Other possible mechanisms include breakthrough by an entirely different scroll wave or a focal source that happens to be active in the area. We also underestimated the frequency of wave breaks because we could not directly detect wave break beneath the surface. The inability to map 3-D impulse propagation also prevented the accurate measurement of conduction velocity, which may be important in the generation and maintenance of wave break (4). Another limitation is that we only studied normal excitable tissue without apparent anatomic obstacles. Therefore, these results may not be applicable to diseased myocardium.

Wu et al. (34) showed that, in a beating heart, the AP measurements could be distorted by myocardial movement. Although VF is not associated with effective and synchronized contractions, some myocardial movement may be present (32). It was unclear if these small myocardium movements prevented us from accurately studying the characteristics of wave breaks and number of wave fronts in VF. We (22) recently performed an experiment to compare the effects of electromechanical uncouplers such as diacetyl monoximide (DAM) and cytochalasin D (Cyto D) on VF activation patterns. Our results showed that DAM significantly reduced the

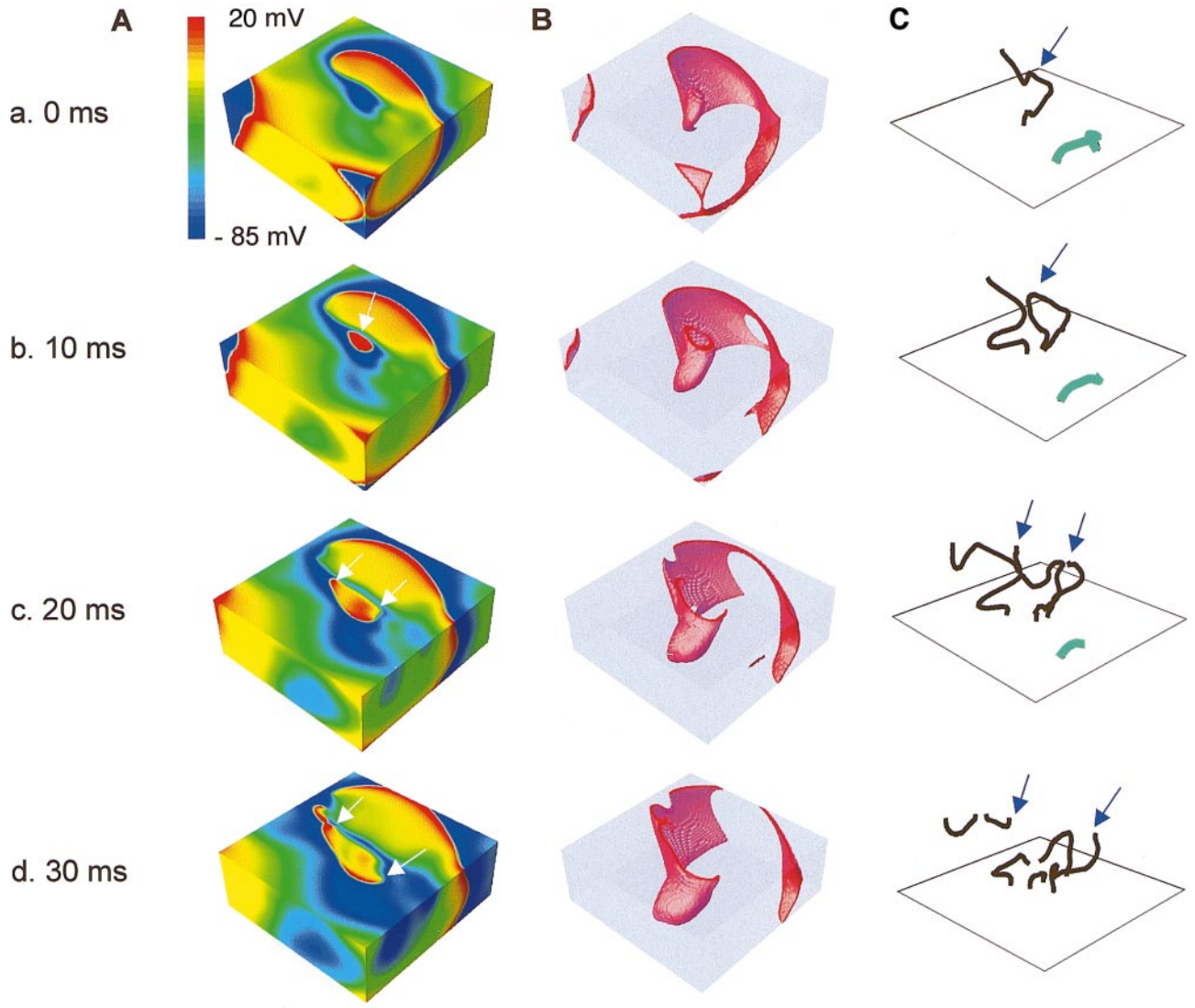

Fig. 10. Three-dimensional simulation of wave break by filament break. *A* and *B*: surface activation patterns (*A*) and the scroll wave fronts in the tissue (*B*). *C*: scroll filaments in the tissue. The black filament developed a severe twist that budded off to form a new scroll ring in C (*frame b*, blue arrow), marking the appearance of the target wave in *A* (*frame b*, white arrow) as the arm of the scroll ring emergeed at the top surface. When the scroll ring filament subsequently arrived at the surface, it broke in two (*C*; *frame c*, blue arrows), apparent on the surface as two new wave breaks (*A*; *frame c*, white arrows). Further breaks in the black filament formed new scroll waves (*C*; *frame c*), whereas the green filament disappeared at the lower border (compare with the experimental wave break in Fig. 6).

slope of APD restitution, the Kolmogorov entropy, and the number of wavelets in VF. On the other hand, the slope of APD restitution curve, the Kolmogorov entropy, and the number of wavelets were the same at baseline (no electromechanical uncoupler) and during Cyto D infusion. These findings suggest that, for optical mapping of VF, electromechanical uncouplers are not needed. However, the same conclusion does not apply to the studies in sinus or paced rhythms, when large movement artifacts may distort the optical image. In those situations, Cyto D (3, 34) is preferable to DAM as an electromechanical uncoupler.

In addition to the above experimental justification for not using an electromechanical uncoupler during the study, our 3-D simulation studies, which are immune to motion artifacts, reproduced all the mechanisms of wave breaks observed in the optical mapping studies. These findings further support the major conclusions of the present study.

The optical signals and the TMP recordings were not exactly the same (Fig. 7). Movement artifacts could partially account for the differences. In addition, the TMP recordings were made with a standard glass microelectrode that registers the TMP from a single cell. In contrast, the optical signals included the activations from multiple cells. Because the activation patterns in VF are complex, neighboring cells may be activated by different wave fronts. Therefore, recordings from a single cell and from a group of cells may look different.

In conclusion, during VF, wave break occurs when wave fronts encounter residual refractoriness left over

from a previous wave or when a scroll wave filament arrives at the surface and breaks. These two fundamental mechanisms are sufficient to explain all of the surface patterns of wave break observed experimentally during sustained VF in normal swine RV.

We thank Ling-Tao Fan, Avile McCullen, Meiling Yuan, and Lucas Huang for technical assistance and Elaine Lebowitz for administrative assistance.

This study was done during the tenure of a Fellowship Grant from the College of Medicine, Yonsei University, Seoul, Korea (to M.-H. Lee). This study was supported in part by a Myung Sun Kim Memorial Foundation Grant (to M.-H. Lee), a Cedars-Sinai Electrocardiographic Heartbeat Organization Foundation Award (to H. S. Karagueuzian), the Kawata and Laubisch Endowments (to J. N. Weiss), a Pauline and Harold Price Endowment (to P.-S. Chen), National Heart, Lung, and Blood Institute Grants P50-HL-52319, R01-HL-58533, and R01-HL-66389, American Heart Association National Center Grants-in-Aid 9750623N and 9950464N, a University of California-Tobacco Related Diseases Research Program 6RT-0020, and the Ralph M. Parsons Foundation, Los Angeles, CA.

REFERENCES

1. **Antzelevitch C, Jalife J, and Moe GK.** Characteristics of reflection as a mechanism of reentrant arrhythmias and its relationship to parasystole. *Circulation* 61: 182–191, 1980.
2. **Athill CA, Ikeda T, Kim YH, Wu T-J, Fishbein MC, Karagueuzian HS, and Chen P-S.** Transmembrane potential properties at the core of functional reentrant wavefronts in isolated canine right atria. *Circulation* 98: 1556–1567, 1998.
3. **Biermann M, Rubart M, Moreno A, Wu J, Josiah-Durant A, and Zipes DP.** Differential effects of cytochalasin D and 2,3-butanedione monoxime on isometric twitch force and transmembrane action potential in isolated ventricular muscle: implications for optical measurements of cardiac repolarization. *J Cardiovasc Electrophysiol* 9: 1348–1357, 1998.
4. **Cao J-M, Qu Z, Kim Y-H, Wu T-J, Garfinkel A, Weiss JN, Karagueuzian HS, and Chen P-S.** Spatiotemporal heterogeneity in the induction of ventricular fibrillation by rapid pacing: importance of cardiac restitution properties. *Circ Res* 84: 1318–1331, 1999.
5. **Cha Y-M, Birgersdotter-Green U, Wolf PL, Peters BB, and Chen P-S.** The mechanisms of termination of reentrant activity in ventricular fibrillation. *Circ Res* 74: 495–506, 1994.
6. **Chen P-S, Wolf PD, Dixon EG, Danieley ND, Frazier DW, Smith WM, and Ideker RE.** Mechanism of ventricular vulnerability to single premature stimuli in open-chest dogs. *Circ Res* 62: 1191–1209, 1988.
7. **Cox JL, Canavan TE, Schuessler RB, Cain ME, Lindsay BD, Stone C, Smith PK, Corr PB, and Boineau JB.** The surgical treatment of atrial fibrillation. II. Intraoperative electrophysiologic mapping and description of the electrophysiologic basis of atrial flutter and atrial fibrillation. *J Thorac Cardiovasc Surg* 101: 406–426, 1991.
8. **Davidenko JM, Persow AV, Salomonza R, Baxter W, and Jalife J.** Sustained vortex-like waves in normal isolated ventricular muscle. *Proc Natl Acad Sci USA* 355: 349–351, 1990.
9. **Davidenko JM, Pertsov AM, Salomonsz R, Baxter W, and Jalife J.** Stationary and drifting spiral waves of excitation in isolated cardiac tissue. *Nature* 355: 349–351, 1992.
10. **Davidenko JM, Salomonsz R, Pertsov AM, Baxter WT, and Jalife J.** Effects of pacing on stationary reentrant activity. Theoretical and experimental study. *Circ Res* 77: 1166–1179, 1995.
11. **Fenton F and Karma A.** Vortex dynamics in three-dimensional continuous myocardium with fiber rotation: filament instability and fibrillation. *Chaos* 8: 20–47, 1998.
12. **Gray RA, Pertsov AM, and Jalife J.** Incomplete reentry and epicardial breakthrough patterns during atrial fibrillation in the sheep heart. *Circulation* 94: 2649–2661, 1996.
13. **Gray RA, Pertsov AM, and Jalife J.** Spatial and temporal organization during cardiac fibrillation. *Nature* 392: 75–78, 1998.
14. **Karagueuzian HS, Khan SS, Hong K, Kobayashi Y, Denton T, Mandel WJ, and Diamond GA.** Action potential alternans and irregular dynamics in quinidine-intoxicated ventricular muscle cells. Implications for ventricular proarrhythmia. *Circulation* 87: 1661–1672, 1993.
15. **Karma A.** Electrical alternans and spiral wave breakup in cardiac tissue. *Chaos* 4: 461–472, 1994.
16. **KenKnight BH, Bayly PV, Gerstle RJ, Rollins DL, Wolf PD, Smith WM, and Ideker RE.** Regional capture of fibrillating ventricular myocardium: evidence of an excitable gap. *Circ Res* 77: 849–855, 1995.
17. **Kim Y-H, Garfinkel A, Ikeda T, Wu T-J, Athill CA, Weiss JN, Karagueuzian HS, and Chen P-S.** Spatiotemporal complexity of ventricular fibrillation revealed by tissue mass reduction in isolated swine right ventricle. Further evidence for the quasiperiodic route to chaos hypothesis. *J Clin Invest* 100: 2486–2500, 1997.
18. **Kim Y-H, Xie F, Yashima M, Wu T-J, Valderrábano M, Lee M-H, Ohara T, Voroshilovsky O, Doshi RN, Fishbein MC, Qu Z, Garfinkel A, Weiss JN, Karagueuzian HS, and Chen P-S.** Role of papillary muscle in the generation and maintenance of reentry during ventricular tachycardia and fibrillation in isolated swine right ventricle. *Circulation* 100: 1450–1459, 1999.
19. **Konings KTS, Kirchhof CJHJ, Smeets JLRM, Wellens HJJ, Penn OC, and Allessie MA.** High-density mapping of electrically induced atrial fibrillation in humans. *Circulation* 89: 1665–1680, 1994.
20. **Krinsky VI.** Spread of excitation in an inhomogeneous medium. *Biophys J* 11: 776–784, 1966.
21. **Lee JJ, Kamjoo K, Hough D, Hwang C, Fan W, Fishbein MC, Bonometti C, Ikeda T, Karagueuzian HS, and Chen P-S.** Reentrant wave fronts in Wiggers' stage II ventricular fibrillation: characteristics, and mechanisms of termination and spontaneous regeneration. *Circ Res* 78: 660–675, 1996.
22. **Lee M-H, Lin S-F, Ohara T, Omichi C, Chudin E, Garfinkel A, Weiss JN, Karagueuzian HS, and Chen P-S.** The effects of diacetyl monoxime and cytochalasin D on action potential restitution and the dynamics of ventricular fibrillation in isolated swine right ventricles. *Am J Physiol Heart Circ Physiol* 280: H2689–H2696, 2001.
23. **Lin S-F, Roth BJ, and Wikswo JP Jr.** Quatrefoil reentry in myocardium: an optical imaging study of the induction mechanism. *J Cardiovasc Electrophysiol* 10: 574–586, 1999.
24. **Luo CH and Rudy Y.** A model of the ventricular cardiac action potential. Depolarization, repolarization, and their interaction. *Circ Res* 68: 1501–1526, 1991.
25. **Mandapati R, Asano Y, Baxter WT, Gray R, Davidenko J, and Jalife J.** Quantification of effects of global ischemia on dynamics of ventricular fibrillation in isolated rabbit heart. *Circulation* 98: 1688–1696, 1998.
26. **Moe GK, Rheinboldt WL, and Abildskov JA.** A computer model of atrial fibrillation. *Am Heart J* 64: 200–220, 1964.
27. **Pertsov AM, Davidenko JM, Salomonsz R, Baxter WT, and Jalife J.** Spiral waves of excitation underlie reentrant activity in isolated cardiac muscle. *Circ Res* 72: 631–650, 1993.
28. **Qu Z and Garfinkel A.** An advanced algorithm for solving partial differential equation in cardiac conduction. *IEEE Trans Biomed Eng* 46: 1166–1168, 1999.
29. **Qu Z, Weiss JN, and Garfinkel A.** Cardiac electrical restitution properties and stability of reentrant spiral waves: a simulation study. *Am J Physiol Heart Circ Physiol* 276: H269–H283, 1999.
30. **Salzberg BM, Davila HV, and Cohen LB.** Optical recording of impulses in individual neurones of an invertebrate central nervous system. *Nature* 246: 508–509, 1973.
31. **Weiss JN, Garfinkel A, Karagueuzian HS, Qu Z, and Chen P-S.** Chaos and the transition to ventricular fibrillation: a new approach to antiarrhythmic drug evaluation. *Circulation* 99: 2819–2826, 1999.
32. **Wiggers CJ.** The mechanism and nature of ventricular fibrillation. *Am Heart J* 20: 399–412, 1940.
33. **Winfree AT.** Spiral waves of chemical activity. *Science* 175: 634–636, 1972.
34. **Wu J, Biermann M, Rubart M, and Zipes DP.** Cytochalasin D as excitation-contraction uncoupler for optically mapping action potentials in wedges of ventricular myocardium. *J Cardiovasc Electrophysiol* 9: 1336–1347, 1998.